Journal of Materials Chemistry A

Accepted Manuscript

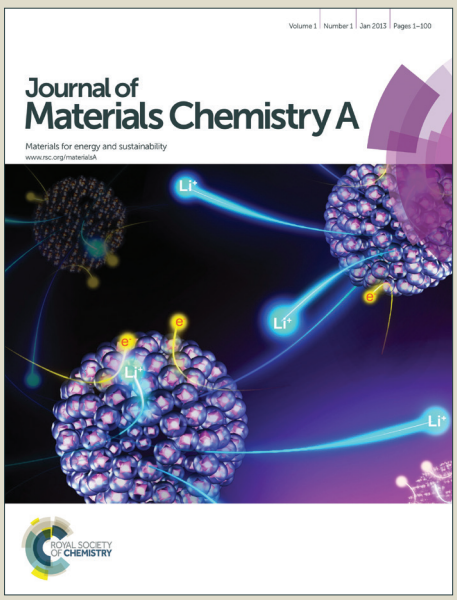

ROYAL SOCIETY OF CHEMISTRY

www.rsc.org/materialsA

Low Lattice Thermal Conductivity in $Pb_5Bi_6Se_{14}$, $Pb_3Bi_2S_6$, and $PbBi_2S_4$: Promising Thermoelectric Materials in the Cannizzarite, Lillianite, and Galenobismuthite Homologous Series

Michihiro Ohta[1,2], Duck Young Chung[1], Masaru Kunii[2], Mercouri G. Kanatzidis[1,3,*]

[1]Materials Science Division, Argonne National Laboratory, Argonne, Illinois 60439, USA

[2]Energy Technology Research Institute, National Institute of Advanced Industrial Science and Technology (AIST), Tsukuba, Ibaraki 305-8568, JAPAN

[3]Department of Chemistry, Northwestern University, Evanston, Illinois 60208, USA

[*]Corresponding Author

E-mail: m-kanatzidis@northwestern.edu (M.G.K)

Abstract

The thermoelectric properties of $Pb_5Bi_6Se_{14}$, a member of the cannizzarite homologous series; $Pb_3Bi_2S_6$, a member of the lillianite homologous series; and $PbBi_2S_4$, a member of the galenobismuthite series were investigated over the temperature range of 300 K to 723 K. The samples were synthesized by a solid state reaction of the binary precursors PbQ and Bi_2Q_3 (Q = S, Se) in evacuated and sealed quartz tubes, followed by pulsed electric current sintering. The crystal structure of $Pb_5Bi_6Se_{14}$ consists of alternating two-dimensional infinite layers of PbSe and Bi_2Se_3. In the $Pb_5Bi_6Se_{14}$ sintered compacts, the *ab*-plane was preferentially oriented perpendicular to the pressing direction, resulting in highly anisotropic electrical and thermal transport properties. The crystal structure of $Pb_3Bi_2S_6$ is formed by stacking NaCl-type (Pb/Bi)S layers with a mirror as twinning operation, while that of $PbBi_2S_4$ consists of the NaCl-type and Bi_2S_3-type strips (broken layers) of finite widths. The crystal grains of $Pb_3Bi_2S_6$ and $PbBi_2S_4$ were grown randomly, leading to nearly isotropic electrical and thermal transport properties in the sintered compacts. For all samples, an *n*-type degenerate semiconductor-like behavior was found, providing a notable thermoelectric power factor of ~3.0 $\mu W\ K^{-2}\ cm^{-1}$ at 705 K for $Pb_5Bi_6Se_{14}$, ~2.4 $\mu W\ K^{-2}\ cm^{-1}$ at 715 K for $Pb_3Bi_2S_6$, and ~2.6 $\mu W\ K^{-2}\ cm^{-1}$at 515 K for $PbBi_2S_4$ in direction perpendicular to the pressing direction. Moreover, these materials exhibited effective phonon scattering, presumably at the interfaces between layers, leading to extremely low lattice thermal conductivity in the range of 0.29 $W\ K^{-1}\ m^{-1}$ to 0.80 $W\ K^{-1}\ m^{-1}$ over the temperature range of 300 K to 723 K. The highest *ZT* of ~0.46 at 705 K was observed in $Pb_5Bi_6Se_{14}$ for the *ab*-plane direction.

1. Introduction

An enormous amount of waste heat generated from various sources could be converted to useful electrical energy to improve energy management and sustainability. Because the heat can be directly converted to electrical energy using thermoelectric generators, it promises waste heat recovery in vehicle exhaust, industrial processes, fuel combustion, and so on. A thermoelectric generator is a solid state device that consists mainly of *p*- and *n*-type semiconductors (thermoelectric materials) and its performance depends on the thermoelectric figure of merit (*ZT*). The efficiency of a thermoelectric material increases with increasing *ZT*, defined as $ZT = \sigma S^2 T/\kappa_{total}$, where σ is the electrical conductivity, S is the Seebeck coefficient, T is the temperature, and κ_{total} is the total thermal conductivity. The quantity σS^2, which is known as the thermoelectric power factor, is the key to achieving high electrical performance and can be optimized by tuning the carrier concentration of materials. The κ_{total} is a combined property by two parts, $\kappa_{total} = \kappa_{el} + \kappa_{lat}$: the electronic thermal conductivity (κ_{el}) and lattice thermal conductivity (κ_{lat}). The former is directly related to the electrical conductivity through the Wiedemann–Franz relation: $\kappa_{el} = LT\sigma$, where L is the Lorenz number. Thus, one strategy to reduce the κ_{total} is to minimize κ_{lat} which is a carrier-independent parameter.

The most widely used thermoelectric materials are Bi_2Te_3–Sb_2Te_3 for near-room-temperature applications and PbTe for intermediate-temperature (~700 K) applications.[1] The *ZT* of PbTe-based materials had been limited to about unity until 2000 but has been dramatically enhanced over 2.0 by nanostructuring.[2–14] The nanostructuring results in a significant reduction in κ_{lat}, allowing an enhancement in the *ZT*. Recently, efforts have been devoted to develop high-*ZT* thermoelectric materials using nanolayered structure approaches (for example, cobalt oxides[15–18], titanium disulfide[18–21], and tin selenide[22]).

The homologous series of layered compounds are great places to look for new classes of thermoelectric materials. A structure of the homologous series is built on the same structural principle with certain module(s) expanding in various dimension(s) by regular increments.[23–26] Therefore, in such homologous compounds, the thermoelectric properties can be tuned by modifying the structural module(s). In the past decade, several homologous layered structures have been reported, including $A_m[M'_{1+l}Se_{2+l}]_{2m}[M''_{2l+n}Se_{2+3l+n}]$ (A = alkali,

alkali earth element; M', M'' = main group element)[27–38], $Cs_4[Bi_{2n+4}Te_{3n+6}]$[28,39–41], $CsM_mBi_3Te_{5+m}$[42,43], and tetradymite homologous series $[MTe]_n[Bi_2Te_3]_m$ (M = Ge, Sn, Pb)[44–52]. A record high *ZT* below room temperature was found in $CsBi_4Te_6$ with ~0.8 at 225 K.[39] In this study, we assessed for the first time the high-temperature thermoelectric properties of $Pb_5Bi_6Se_{14}$, a member of the cannizzarite homologous series; $Pb_3Bi_2S_6$, a member of the lillianite homologous series; and $PbBi_2S_4$, a member of the galenobismuthite series.

$Pb_5Bi_6Se_{14}$ originates from the mineral cannizzarite ($Pb_{46}Bi_{54}S_{127}$)[23–26,53] and is a member (n = 1, m = 1) of the cannizzarite homologous series with a general formula $[(PbSe)_5]_n[(Bi_2Se_3)_3]_m$, in which two different module layers PbSe and Bi_2Se_3 are Pb/Bi mixed occupied. As shown in Figure 1(a), the crystal structure of $Pb_5Bi_6Se_{14}$ consists of alternating infinite PbSe- and Bi_2Se_3-type layers.[54] The two layers are stacked alternately along *c*-axis to build a three-dimensional structure and vary their thickness to form different members in the homology. This natural planar superlattice structural feature prompted us to investigate the thermoelectric properties of $Pb_5Bi_6Se_{14}$. Recently, Shelimova *et al.*[55,56] measured the thermoelectric properties of three members of cannizzarite homologous series $Pb_5Bi_6Se_{14}$, $Pb_5Bi_{12}Se_{23}$, and $Pb_5Bi_{18}Se_{32}$ over the temperature range of 80 K to 370 K. The melt-grown ingots of all systems showed low value of κ_{lat}; for example room-temperature κ_{lat} of $Pb_5Bi_6Se_{14}$ was 0.72 W K^{-1} m^{-1}. Interestingly, it was recently found that Ag doping of $Pb_5Bi_{12}Se_{23}$ results in superconductivity.[57] In order to evaluate their potential for thermoelectric applications, the high-temperature thermoelectric properties of the cannizzarite homologous series should be investigated on highly oriented samples. These investigations provide insights for achieving high *ZT* in the cannizzarite homologous series.

$Pb_3Bi_2S_6$ is a member of the lillianite homologous series, of which the crystal structure is formed by stacking NaCl-type (Pb/Bi)S layers with a mirror as twinning operation,[23,26,58–61] as shown in Figure 1(b). The members of the lillianite series evolve by the thickness of the (Pb/Bi)S layers. $PbBi_2S_4$ belongs to the galenobismuthite homologous series with an isostructural crystal structure to $CaFe_2O_4$.[23,26,62–64] In the crystal structure, the NaCl- and Bi_2S_3-type layers are broken into strips of finite widths (Figure 1(c)). Like the cannizzarite homologous series, the complex crystal structures of the lillianite and galenobismuthite homologous series are expected to yield the low lattice thermal conductivity and two lillianite members

$K_xSn_{6-2x}Bi_{2+x}Se_9$ and $KSn_5Bi_5Se_{13}$ were measured only for the near-room-temperature σ and S.[65]

In this paper, we report the high-temperature thermoelectric properties of the cannizzarite homologous member $Pb_5Bi_6Se_{14}$, the lillianite homologous member $Pb_3Bi_2S_6$, and the galenobismuthite member $PbBi_2S_4$. The σ, S, and κ_{total} of their sintered compacts were measured perpendicular (in-plane) and parallel (out-of-plane) to the pressing direction over the temperature range of 300 K to 723 K. While anisotropic electrical and thermal transport properties were found in $Pb_5Bi_6Se_{14}$, nearly isotropic electrical and thermal transport properties were found in $Pb_3Bi_2S_6$ and $PbBi_2S_4$. We demonstrate a notable power factor, σS^2 and an extremely low κ_{lat} in $Pb_5Bi_6Se_{14}$, $Pb_3Bi_2S_6$, and $PbBi_2S_4$. The strategy for achieving high ZT in these homologous series is discussed.

2. Experimental Section

2.1. Synthesis

Elemental lead (Pb; 99.9999%, Osaka Asahi Metal MFG), elemental bismuth (Bi; 99.9999%, Osaka Asahi Metal MFG), elemental selenium (Se; 99.999%, Kojundo Chemical Laboratory), and elemental sulfur (S; 99.9999%, Kojundo Chemical Laboratory) were used as starting materials without further purification. Binary chalcogenides PbSe, PbS, Bi_2Se_3, and Bi_2S_3 were prepared first. Ternary chalcogenides $Pb_5Bi_6Se_{14}$, $Pb_3Bi_2S_6$, and $PbBi_2S_4$ were then prepared by a solid state reaction from the binary chalcogenides.

2.1.1. $Pb_5Bi_6Se_{14}$

In the preparation of binary precursor PbSe, a stoichiometric mixture of elements with a total mass of ~10 g was loaded into a fused silica tube of 12 mm outer diameter × 10 mm inner diameter. The tube was evacuated to a pressure of ~10^{-3} Pa and then flame-sealed. The mixture was heated to 773 K at a rate of ~40 K h^{-1}, heated to 1393 K at a rate of ~80 K h^{-1}, and then held at 1393 K for 12 h. The sample was then cooled to room temperature over 2 h.

In the preparation of Bi_2Se_3 starting material, a stoichiometric amount of Bi and Se with a total mass of ~10 g was loaded into a fused silica tube of 12 mm outer diameter × 10 mm inner diameter. The tube was evacuated to a pressure of ~10^{-3} Pa and then flame-sealed. The mixture was heated to 773 K at a rate of ~40 K h^{-1}, heated to 1173 K at a rate of ~60 K h^{-1}, and then held at 1173 K for 12 h. The sample was then cooled to room temperature over 2 h.

For the preparation of $Pb_5Bi_6Se_{14}$, the melt grown ingots of PbSe and Bi_2Se_3 were hand-ground. A stoichiometric amount of PbSe (4.214 g) and Bi_2Se_3 (5.786 g) powders with a total mass of 10 g was well mixed and loaded into a fused silica tube of 12 mm outer diameter × 10 mm inner diameter. The tube was evacuated to a pressure of ~10^{-3} Pa and then flame-sealed. The mixture was heated to 873 K at a rate of ~290 K h^{-1}, held at 873 K for 120 h, and then slowly cooled to room temperature at a rate of ~20 K h^{-1}. To improve homogeneity of the product, the powder obtained was thoroughly mixed and heating repeatedly under the same condition at 873 K for 120 h. The total reaction time was 240 h.

2.1.2. $Pb_3Bi_2S_6$ and $PbBi_2S_4$

A pre-process for the binary precursors PbS and Bi_2S_3 are same as above. The stoichiometric mixture of Pb and S was loaded into a carbon-coated fused silica tubes. The tubes were evacuated to a pressure of ~10^{-3} Pa and then flame-sealed. The reaction mixture was heated to 773 K at a rate of ~40 K h^{-1}, heated to 1423 K at a rate of ~80 K h^{-1}, and then held at 1423 K for 12 h before cooling to room temperature over 2 h. The stoichiometric mixture of Bi and S loaded into a sealed fused silica tube was heated to 773 K at a rate of ~40 K h^{-1}, heated to 1223 K at a rate of ~60 K h^{-1}, and then held at 1223 K for 12 h before cooling to room temperature over 2 h.

For the preparation of $Pb_3Bi_2S_6$, the melt grown ingots of binary chalcogenides PbS and Bi_2S_3 were hand-ground. A stoichiometric ratio of PbS (5.826 g) and Bi_2S_3 (4.174 g) with a total mass of 10 g was well mixed and then loaded into a fused silica tube of 12 mm outer diameter × 10 mm inner diameter. The tube was evacuated to a pressure of ~10^{-3} Pa and then flame-sealed. The mixture was heated to 973 K at a rate of ~340

K h^{-1}, held at 973 K for 120 h, and then slowly cooled to room temperature at a rate of ~30 K h^{-1}. Annealing was repeated at the same temperature after grinding/mixing powder obtained to improve homogeneity of the product. The total reaction time was 240 h.

A same procedure was applied for the preparation of $PbBi_2S_4$ with a stoichiometric amount of hand-ground PbS (3.176 g) and Bi_2S_3 (6.824 g) with a total mass of 10 g. The mixture was heated to 973 K at a rate of ~340 K h^{-1}, held at 973 K for 120 h, and then slowly cooled to room temperature at a rate of ~30 K h^{-1} in a vacuum-sealed silica tube. This annealing step was repeated to improve homogeneity of the powder obtained. The total reaction time was 240 h.

2.2. Sintering

The samples were sintered under a uniaxial pressure to obtain the dense compacts. The powders of ternary chalcogenides $Pb_5Bi_6Se_{14}$, $Pb_3Bi_2S_6$, and $PbBi_2S_4$ prepared above were re-ground to pass through a 20 μm size sieve and then placed into graphite dies. In each material, the graphite die was inserted into the pulsed electric current sintering apparatus (SPS-515S, Fuji Electronic Industrial). For selenide samples, sintering was performed at 823 K for 2 h under a uniaxial pressure of 30 MPa in vacuum (7.0×10^{-3} Pa). For sulfide samples, sintering was performed at 773 K for 2 h under a uniaxial pressure of 30 MPa in vacuum (7.0×10^{-3} Pa). In all cases, the heating and cooling rates were 10 K min^{-1} and 20 K min^{-1}, respectively. In order to improve the homogeneity and prepare the oriented sintered compacts, a 2 h long sintering time was applied.

The mass density of the sintered compacts was determined using the Archimedes method. The sintered density of all samples was found to be greater than 99% of the theoretical density (Table S1 in the Supplementary Information).

For each material, we prepared three sintered samples with different sizes for electrical and thermal transport measurements in the direction of perpendicular (in-plane) and parallel (out-of-plane) to the pressing direction. The cylindrical samples of ~10 mm diameter × ~11 mm length were cut into bars and coins for out-of-plane electrical transport measurements and in-plane thermal transport measurements, respectively. The

disks of ~15 mm diameter × ~ 2mm thickness were cut into bars for in-plane electrical transport measurements. The disks of ~10 mm diameter × ~2 mm thickness were used for out-of-plane thermal transport measurements.

2.3. Powder X-ray Diffraction and Scanning Electron Microscopy

The crystal structure of the synthetic powders and sintered compacts was examined by X-ray diffractometry (XRD; Rint-Ultima+, Rigaku) using the Cu Kα radiations over the 2θ range of 10°–80°. Both in-plane and out-of-plane XRD patterns of the sintered compacts were investigated in order to examine the crystal orientation. The microstructure of the sintered compacts was observed on the fractured sections parallel to the pressure direction by scanning electron microscopy (SEM; JSM-6610LV, JEOL, 20kV).

2.4. Electrical Transport Measurements

The Seebeck coefficient and electrical resistivity were measured simultaneously under He atmosphere using a temperature differential method and four-probe method, respectively (ZEM-3, ULVAC-RIKO) over the temperature range of 300 K to 723 K. The typical dimensions of the bars used for the in-plane measurements were ~3 mm × ~2 mm × ~12 mm and for out-of-plane measurements were ~3 mm × ~3 mm × ~11 mm. Seebeck coefficient and electrical resistivity were reproducible over heating and cooling cycles for all samples.

The Hall coefficient (R_H) of the sintered compacts was measured at room temperature with a home-built system[66] under a magnetic field of 0 T to 2.3 T. The typical sample dimensions were ~5 mm × ~5 mm × ~0.3 mm. The Cu contact wires were attached to the samples using In-rich In-Ga paste. The room-temperature Hall coefficient is given in Table S2 in the Supplementary Information.

2.5. Thermal Transport Measurements

The total thermal conductivity (κ_{total}) was calculated from the thermal diffusivity (D), heat capacity (C_P), and sintered mass density (d) using the expression $\kappa_{total} = DC_Pd$. The thermal diffusivity was directly measured and the heat capacity was indirectly derived using a standard sample (Pyroceram 9606, Netzsch) using the laser flash method (LFA 457 MicroFlash, Netzsch) under the Ar gas flow atmosphere (100 ml min^{-1}) over the temperature range 300 K to 723 K. The samples for in-plane measurements were square plates of ~10 mm × ~10 mm × ~2 mm and the samples for out-of-plane measurements were coins of ~ 10 mm in diameter and ~2 mm in thickness. Graphite spray coating was applied on the sample surface. The thermal diffusivity was reproduced over heating and cooling cycles for all sintered compacts. The thermal diffusivity and heat capacity are provided in Figures S1 and S2 in the Supplementary Information.

The heat capacity was confirmed by measuring the samples in differential scanning calorimetry (DSC; DSC 3500 Sirius, Netzsch) under an N_2 gas flow atmosphere (100 ml min^{-1}) over the temperature range 300 K to 473 K . The typical sample dimensions were ~5 mm × ~5 mm × ~1 mm. In the temperature range 300 K to 473 K, the discrepancy between the values of heat capacity measured in laser flash method and this DSC method is within the measurement error range of ~10% (Figure S2 in the Supplementary Information). The values obtained through laser flash method were used for determining the thermal conductivity over 300 K–723 K.

The sound velocities for longitudinal and transverse modes were measured at room temperature by the pulse-echo method with ultrasonic pulser/receivers (5077PR, Olympus), 5 MHz and 15 MHz longitudinal contact transducers, 5 MHz transverse contact transducers, and digitizing oscilloscope (WaveJet300A, Teledyne LeCroy). The typical dimensions of the square plates used for the in-plane measurements were ~10 mm × ~10 mm × ~2 mm and of the coins used for out-of-plane measurements were ~10 mm in diameter and ~2 mm in thickness.

3. Results and Discussion

3.1. Synthesis and Sintering

The powder X-ray diffraction (XRD) patterns of the samples before and after sintering are shown in Figure 2. In all cases, the synthetic and sintering processes used in this study produced single phases of the monoclinic $Pb_5Bi_6Se_{14}$ ($P2_1/m$)[54] (Figure 2(a)), orthorhombic $Pb_3Bi_2S_6$ ($Cmcm$)[61] (Figure 2(b)), and orthorhombic $PbBi_2S_4$ ($Pnma$)[64] (Figure 2(c)). No secondary phase was observed. Table 1 lists the lattice parameters calculated from the measured powder XRD patterns of $Pb_5Bi_6Se_{14}$, $Pb_3Bi_2S_6$, and $PbBi_2S_4$ before and after sintering and known space groups[54,61,64]. The X-ray diffractometer was calibrated with an external standard of Si. No significant changes of lattice parameters was found after sintering; for example lattice parameters of $Pb_5Bi_6Se_{14}$ are a = 2.1537 nm, b = 0.4202 nm, c = 1.6028 nm, β = 97.34° before sintering and a = 2.1540 nm, b = 0.4206 nm, c = 1.6047 nm, β = 97.39° after sintering.

Figure 2 also shows the out-of-plane XRD patterns for all sintered compacts. For the case of $Pb_5Bi_6Se_{14}$, a strong enhancement of the basal (00l) reflections was observed, showing that the crystalline c-axis is preferentially oriented along the pressing (out-of-plane) direction. The degree of (00l) orientation, referred to as the Lotgering factor f was calculated from the relation $f = [(P-P_0)/(1-P_0)]$ where $P = \sum I(00l)/\sum I(hkl)$, where $\sum I(00l)$ and $\sum I(hkl)$ are the sums of the intensities of (00l) and (hkl) reflections, respectively, and P_0 is the value of P for a randomized powder sample.[67] While a perfectly orientated sample provides f = 1, a randomly orientated one provides f = 0. In this study, the Bragg reflections in the range 10° to 60° were used for calculation of f. The f of out-of-plane XRD pattern of $Pb_5Bi_6Se_{14}$ is ~0.5. On the other hand, the powder and out-of-plane XRD patterns of the sulfide systems ($Pb_3Bi_2S_6$ and $PbBi_2S_4$) are very similar, indicating that these sintered compacts have a low degree of preferred orientation. These conclusions are supported by the results of the scanning electron microscopy (SEM) examinations of the sintered compacts, which is discussed below.

Figure 3 shows SEM micrographs of the fractured section of the sintered compacts (~15 mm diameter × ~2 mm thickness) that were fractured parallel to the pressure direction. The SEM micrographs of three sintered compacts of different sizes in each system are shown in Figure S3–S5. The examination of all the samples by SEM reveals a dense structure, which is consistent with the results of the Archimedes density measurements (Table S1 in the Supplementary Information). In the case of $Pb_5Bi_6Se_{14}$, a well-organized

texture was observed, and the preferential crystal orientation is apparent in the fractured section (Figure 3(a)). The crystal grains were preferentially grown in the direction perpendicular to the pressure applied during sintering, forming the needle-like grains with mean length of ~30 μm. This natural layering of the grains is probably due to the strong intralayer and weak interlayer bonding. In the case of sulfide systems, random textures were observed in Figure 3(b) and (c), meaning that the grains were grown randomly. The mean size of the plate-like grains of both samples is ~10 μm. Based on the orientation of texture observed, $Pb_5Bi_6Se_{14}$ is expected to provide anisotropic electrical and thermal transport properties, while the random texture of $Pb_3Bi_2S_6$ and $PbBi_2S_4$ provides nearly isotropic transport properties.

Since the sintered compacts prepared in this study consist of a single phase of $Pb_5Bi_6Se_{14}$, $Pb_3Bi_2S_6$, and $PbBi_2S_4$ and have a high sintered density (>99%), they are suitable for investigation of their thermoelectric properties.

3.2 Thermoelectric Properties of $Pb_5Bi_6Se_{14}$

The temperature dependences of the electrical conductivity (σ) and Seebeck coefficient (S) for the sintered compacts of $Pb_5Bi_6Se_{14}$ are shown in Figure 4 (a) and (b), respectively. The data are consistent with an *n*-type degenerate semiconductor, namely, the σ decreases while S increases as the temperature increases. The sign of S and the Hall coefficient (Table S2 in the Supplementary Information) is negative, confirming *n*-type carrier transport.

We estimated the carrier concentration (n) from the formula $n = 1/eR_H$, where e represents the electronic charge and R_H is the Hall coefficient. The room-temperature n is given in Table 2 and the R_H is given in Table S2 in the Supplementary Information. The $Pb_5Bi_6Se_{14}$ system was found to have n of 4.8×10^{19} cm^{-3}, which falls in category of degenerate semiconductor.

As shown in Figure 4(a), the σ is highly anisotropic between the in-plane and out-of-plane directions for the whole temperature range measured; for example at 300 K, the in-plane σ value (~157 S cm^{-1}) is nearly 3.5 times higher than out-of-plane σ value (~41.2 S cm^{-1}). The σ is related to n and the carrier mobility (μ) and is

expressed as:

$$\sigma = en\mu \quad . \quad (1)$$

Therefore, the difference in σ originates in the difference in μ. The room-temperature μ was calculated from n and σ and are given in Table 2. For $Pb_5Bi_6Se_{14}$, the in-plane μ value (~20 $cm^2\ V^{-1}\ s^{-1}$) is nearly 3.5 times higher than out-of-plane μ value (~5.4 $cm^2\ V^{-1}\ s^{-1}$). The μ is related to scattering time τ through the e and m^*: $\mu = e\tau/m^*$. Therefore, the low values of σ and μ in out-of-plane direction are principally due to the reduced τ through the significant electron scattering at the interfaces between PbSe and Bi_2Se_3 modular layers.

Unlike the σ, an insensitivity of S to the crystal orientation was observed (Figure 4(b)); for example at 705 K, the in-plane S value (~210 $\mu V\ K^{-1}$) is in rough agreement with out-of-plane S value (~230 $\mu V\ K^{-1}$). To interpret the isotropic S, we used the following formula as an approximation:[1,68,69]

$$S = \frac{8\pi^2 k_B^2}{3eh^2} m^* T \left(\frac{\pi}{3n}\right)^{\frac{2}{3}} \quad , \quad (2)$$

where h is Planck's constant and m^* is the effective mass. This relationship is derived from the parabolic band model and energy-independent scattering time for metals and degenerate semiconductors. No relationship between S and τ were found in Eq. (2), resulting in isotropic behaviour in S.

Figure 4 (c) shows the temperature dependence of the σS^2 of $Pb_5Bi_6Se_{14}$ calculated from the measured σ and S. The highest σS^2 is achieved the in-plane direction, because of the higher σ in the in-plane direction and the insensitivity of S to crystal orientation. At 705 K, the in-plane σS^2 value is ~3.0 $\mu W\ K^{-2}\ cm^{-1}$, which is 47% higher than the out-of-plane σS^2 value (~1.6 $\mu W\ K^{-2}\ cm^{-1}$).

Figure 4 (d) shows the temperature dependence of the total thermal conductivity (κ_{total}) of the $Pb_5Bi_6Se_{14}$ sintered compacts in the in-plane and out-of-plane directions. For both directions, the κ_{total} is quite low and is in the range of 0.33–0.58 $W\ K^{-1}\ m^{-1}$. The very low value of κ_{total} is of great advantage to further develop high-performance thermoelectric materials.

The electronic thermal conductivity (κ_{el}) was estimated using the Wiedemann–Franz relation with the Lorenz number $L = 2.44 \times 10^{-8}\ W\ \Omega\ K^{-2}$ (Sommerfeld value). The lattice thermal conductivity (κ_{lat}) was obtained by subtracting κ_{el} from κ_{total} and is plotted in Figure 4 (d). The κ_{lat} is anisotropic between the in-plane

and out-of-plane directions for the whole temperature range measured; for example at 723 K, the in-plane κ_{lat} (~0.35 W K^{-1} m^{-1}) is ~20% higher than out-of-plane κ_{lat} (~0.29 W K^{-1} m^{-1}).

The κ_{lat} is related to the average sound velocity (v_a), volumetric heat capacity at constant pressure (C_v), mean free path of phonon (l_p) and is expressed as:

$$\kappa_{\mathrm{lat}} = \frac{1}{3} C_{\mathrm{v}} v_a l_{\mathrm{p}} \qquad (3)$$

The v_a is defined as:[70–72]

$$\frac{1}{v_{\mathrm{a}}^3} = \left[\frac{1}{3}\left(\frac{1}{\mathrm{v_l}^3} + \frac{2}{\mathrm{v_t}^3}\right)\right] \qquad (4)$$

Table 3 summarizes the room-temperature longitudinal sound velocity (v_l), transverse sound velocity (v_t) measured by the pulse-echo method, calculated v_a, and estimated l_p of $Pb_5Bi_6Se_{14}$. In this estimation, the C_v was assumed to be equal to measured C_p.[73,74] The in-plane v_l (~2720 m s^{-1}) and v_t (~1220 m s^{-1}) are almost same as the out-of-plane v_l (~2740 m s^{-1}) and v_t (~1210 m s^{-1}). On the other hand, the out-of-plane l_p (0.6 nm) is shorter than the in-plane l_p (0.8 nm). Moreover, the out-of-plane l_p is ~60% shorter than the length of the *c*-axis (1.604 nm, Table 1) and reach the interlayer distance between PbSe and Bi_2Se_3 module layers. The facts mean that the extremely low value of the out-of-plane κ_{lat} for $Pb_5Bi_6Se_{14}$ is attributed to the fact that the interfaces between PbSe layer and Bi_2Se_3 layer effectively scatter the heat-carrying phonons, like the electron scattering.

The theoretical minimum limit of lattice thermal conductivity (κ_{min}) can be written as:[75]

$$\kappa_{min} = \left(\frac{\pi}{6}\right)^{1/3} k_{\mathrm{B}} n_{\mathrm{a}}^{2/3} \sum_i v_i \left(\frac{T}{\Theta_i}\right)^2 \int_0^{\Theta_i/T} \frac{x^3 e^x}{(e^x-1)} dx \qquad (5)$$

The v_i, Θ_i, and n_a are the sound velocity associated to the longitudinal and transverse modes, Debye temperature associated to these modes, and the number density of atoms, respectively. Θ_i is related to v_i and n_a and is expressed as:[75]

$$\Theta_i = v_i \left(\frac{\hbar}{k_B}\right) (6\pi^2 n_{\mathrm{a}})^{1/3} \qquad (6)$$

The room-temperature κ_{min} is plotted in Figure 4 (d) and the longitudinal Θ_l and transverse Θ_t are shown in Table 3. As shown in Figure 4 (d), the κ_{min} is less than in-plane and out-of-plane κ_{lat}. The results suggest that

there is room for reduction in κ_{lat} through increasing complexity of crystal structure/introducing disorder to matrix. This may be achieved by the crystal structural evolution from $[(PbSe)_5][(Bi_2Se_3)_3]$ to $[(PbSe)_5][(Bi_2Se_3)_6]$ and $[(PbSe)_5][(Bi_2Se_3)_9]$.[25]

Figure 5 shows the thermoelectric figure of merit (ZT) of the $Pb_5Bi_6Se_{14}$ sintered compacts in the in-plane and out-of-plane directions calculated from the measured σ, S, and κ_{total}. The highest ZT of 0.46 was observed at 705 K for the in-plane direction, because it possesses the highest σS^2. The ZT can be further boosted by following strategies; the tuning of n through doping for optimizing σS^2, microstructure tuning and single-crystal growth for increasing μ, and crystal structural evolution for reducing κ_{lat}.

It is interesting to compare the thermoelectric properties observed in this study with those observed in the previous study[55]. As shown in Table 4, the n of the sintered sample prepared in this study is lower than that of the melt-grown ingot prepared previously, allowing higher σS^2. Moreover, the oriented texture and effective phonon scattering at grain boundaries in the sintered sample lead to lower κ_{lat} and κ_{total}. Therefore, the higher ZT was found in the material of this study.

3.3 Thermoelectric Properties of $Pb_3Bi_2S_6$ and $PbBi_2S_4$

Figures 6(a), (b) and (c) and Figures 7(a), (b), and (c) show the temperature dependence of the electrical conductivity (σ), Seebeck coefficient (S), and power factor (σS^2) of $Pb_3Bi_2S_6$ and $PbBi_2S_4$, respectively. The data of both samples are consistent with an n-type degenerate semiconductor. The sign of the Hall coefficient confirms the n-type carrier transport (Table S2 in Supplementary Information).

As given in Table 2, the room-temperature carrier concentration (n) for the $Pb_3Bi_2S_6$ and $PbBi_2S_4$ samples were found to be 1.2×10^{20} cm^{-3} and 4.6×10^{19} cm^{-3}, respectively. Like $Pb_5Bi_6Se_{14}$, the values fall in degenerate semiconductors.

The room-temperature carrier mobilities (μ) were calculated from n and σ by using Eq. (1) and are given in Table 2. There are no significant differences observed in σ and μ between the in-plane and out-of-plane directions of $Pb_3Bi_2S_6$ and $PbBi_2S_4$ for the whole temperature range measured (Figure 6(a) and Figure 7(a)).

For $Pb_3Bi_2S_6$ at 300 K, the in-plane σ (~193 S cm^{-1}) and μ (~9.9 cm^2 V^{-1} s^{-1}) are slightly less than the out-of-plane σ (~219 S cm^{-1}) and μ (~11 cm^2 V^{-1} s^{-1}). For $PbBi_2S_4$ at 300 K, the in-plane σ (~68.2 S cm^{-1}) and μ (~9.3 cm^2 V^{-1} s^{-1}) are slightly less than the out-of-plane σ (~89.4 S cm^{-1}) and μ (~12 cm^2 V^{-1} s^{-1}). Unlike $Pb_5Bi_6Se_{14}$, the more random textures of $Pb_3Bi_2S_6$ and $PbBi_2S_4$ samples lead to nearly isotropic electrical transport properties.

Like the behavior in σ, there are no significant differences in S between the in-plane and out-of-plane directions for $Pb_3Bi_2S_6$ (Figure 6(b)) and $PbBi_2S_4$ (Figure 7(b)). For $Pb_3Bi_2S_6$ at 715 K, the in-plane S (~−200 μV K^{-1}) is slightly larger than out-of-plane S value (~−180 μV K^{-1}). For $PbBi_2S_4$ at 710 K, the in-plane S (~−290 μV K^{-1}) is slightly larger than out-of-plane S value (~−270 μV K^{-1}).

The σS^2 of the $Pb_3Bi_2S_6$ and $PbBi_2S_4$ samples are shown in Figure 6(c) and Figure 7(c), respectively. As a collective property, σS^2 also has no significant difference between the in-plane and out-of-plane directions for $Pb_3Bi_2S_6$ and $PbBi_2S_4$. For $Pb_3Bi_2S_6$, the in-plane σS^2 increases with increasing temperature, reaching a maximum of ~2.4 μW K^{-2} cm^{-1} at 715 K. For $PbBi_2S_4$, the out-of-plane σS^2 increases from ~1.6 μW K^{-2} cm^{-1} at 300 K to maximum of ~2.7 μW K^{-2} cm^{-1} at 610 K and decreases slightly to ~2.6 μW K^{-2} cm^{-1} at 710 K as the temperature increases. The σS^2 for $Pb_3Bi_2S_6$ and $PbBi_2S_4$ is slightly less than the in-plane σS^2 for $Pb_5Bi_6Se_{14}$ (~3.0 μW K^{-2} cm^{-1} at 705 K, Figure 4(c)).

Figure 6(d) and Figure 7(d) show the temperature dependence of the total thermal conductivity (κ_{total}) of $Pb_3Bi_2S_6$ and $PbBi_2S_4$ sintered compacts, respectively, in the in-plane and out-of-plane directions. Like electrical transport properties, the nearly isotropic thermal transport properties were observed for both systems. The sintered compacts of $Pb_3Bi_2S_6$ and $PbBi_2S_4$ show very low value of κ_{total}, which is of great advantage as thermoelectric materials. At 723 K, the in-plane κ_{total} was found to be 0.67 W K^{-1} m^{-1} for $Pb_3Bi_2S_6$ and to be 0.57 W K^{-1} m^{-1} for $PbBi_2S_4$.

The electrical thermal conductivity (κ_{el}) is estimated using the Wiedemann–Franz relation with the Sommerfeld L. The lattice thermal conductivity (κ_{lat}) was obtained by subtracting κ_{el} from κ_{total} is plotted in Figure 6(d) for $Pb_3Bi_2S_6$ and Figure 7(d) for $PbBi_2S_4$. Both sintered compacts show extremely low values of $\kappa_{lat,}$ which is less than 0.79 W K^{-1} m^{-1} for $Pb_3Bi_2S_6$ and less than 0.63 W K^{-1} m^{-1} for $PbBi_2S_4$.

Table 3 summarizes the room-temperature longitudinal sound velocity (v_l), transverse sound velocity (v_t), average sound velocity (v_a), and mean free path of phonon (l_p) of $Pb_3Bi_2S_6$ and $PbBi_2S_4$. In the case of all the systems, the in-plane v_l and v_t are almost the same as the out-of-plane v_l and v_t. The important point here is that all the l_p are shorter than the length of the *c*-axes (Table 1) reach the interlayer distances of twin layers in $Pb_3Bi_2S_6$ and strips in $PbBi_2S_4$. These results suggest that the extremely low values of κ_{lat} are attributed to the interfaces between twin layers in $Pb_3Bi_2S_6$ or strips in $PbBi_2S_4$ which effectively scatter the heat-carrying phonons.

The room-temperature κ_{min} is plotted in Figure 4(d) and the longitudinal Θ_l and transverse Θ_t are shown in Table 3. The κ_{min} is less than the in-plane and out-of-plane κ_{lat}, suggesting a possibility for further reduction of k_{lat}. Like $Pb_5Bi_6Se_{14}$, future reduction in k_{lat} through increasing complexity of crystal structure is probably achieved by the crystal structural evolution (for example, layered structure built up from $Pb_3Bi_2S_6$ to $Pb_6Bi_2S_9$[23,26]).

Figure 8 and Figure 9 show the thermoelectric figure of merit (*ZT*) of the $Pb_3Bi_2S_6$ and $PbBi_2S_4$ sintered compacts in the in-plane and out-of-plane directions calculated from the measured σ, *S*, and κ_{total}, respectively. There are no significant differences in *ZT* between the in-plane and out-of-plane directions for both samples. For $Pb_3Bi_2S_6$, the in-plane *ZT* increases with increasing temperature, reaching a maximum of 0.26 at 715 K. For $PbBi_2S_4$, the out-of-plane *ZT* increases from 0.08 at 300 K to maximum of 0.33 at 710 K as the temperature increases. The *ZT* values of $Pb_3Bi_2S_6$ and $PbBi_2S_4$ are lower than that for $Pb_5Bi_6Se_{14}$ (Figure 4(c)), because of lower σS^2 and higher κ_{total}. Like $Pb_5Bi_6Se_{14}$, the *ZT* of $Pb_3Bi_2S_6$ and $PbBi_2S_4$ can be further improved by the tuning of *n* through doping for optimizing σS^2, microstructure tuning and single-crystal growth for increasing μ, and crystal structural evolution for reducing κ_{lat}.

Finally, as this paper was being reviewed a narrow gap semiconductor $Pb_7Bi_4Se_{13}$ was reported to crystallize in the monoclinic space group *C*2/*m* (a member of the lillianite series) possessing a very low thermal conductivity (~0.33 W m^{-1} K^{-1} at 300 K). This adds to the collection of compounds described here and points to the Pb-Bi-Q (Q =S, Se, Te) class as a promising set of potentially important thermoelectric materials.[76]

3.4 Comparison between $Pb_5Bi_6Se_{14}$, $Pb_3Bi_2S_6$ and $PbBi_2S_4$

Finally, we compare the thermoelectric properties of $Pb_5Bi_6Se_{14}$ with those of $Pb_3Bi_2S_6$ and $PbBi_2S_4$. In the $Pb_5Bi_6Se_{14}$ sintered compacts, the *c*-plane was preferentially oriented parallel to the out-of-plane direction, resulting in highly anisotropic electrical and thermal transport properties. The in-plane σS^2 is higher than the out-of-plane σS^2, because of the higher σ in the in-plane direction and the insensitivity of S to crystal orientation. Moreover, the in-plane κ_{lat} is higher than out-of-plane κ_{lat}. Because of higher σS^2 in the in-plane direction, the highest ZT of 0.46 was observed at 705 K for the in-plane direction.

The crystal grains of $Pb_3Bi_2S_6$ and $PbBi_2S_4$ were grown randomly, leading to nearly isotropic electrical and thermal transport properties in the sintered compacts. There are no significant differences observed in σS^2, κ_{lat}, and ZT between the in-plane and out-of-plane directions for the whole temperature range measured. The ZT values increase with increasing temperature, reaching a maximum of 0.26 at 715 K for in-plane direction in $Pb_3Bi_2S_6$ and 0.33 at 710 K for the out-of-plane direction in $PbBi_2S_4$. The ZT values of $Pb_3Bi_2S_6$ and $PbBi_2S_4$ are lower than that for $Pb_5Bi_6Se_{14}$, because of lower σS^2 and higher κ_{total}.

4. Concluding remarks

We investigated for the first time the high-temperature thermoelectric properties of the cannizzarite homologous member $Pb_5Bi_6Se_{14}$, lillianite homologous member $Pb_3Bi_2S_6$, and galenobismuthite homologous member $PbBi_2S_4$. The layered structures of these systems yield very low lattice thermal conductivity in the range of 0.30 to 0.81 W K^{-1} m^{-1} over the temperature range of 300 to 723 K, because the interfaces between layers effectively scatter the heat-carrying phonons. Moreover, all samples are *n*-type degenerate semiconductors. The very low lattice thermal conductivity and degenerate semiconductor-like behavior are of great advantages to further develop high-performance thermoelectric materials. The highest thermoelectric figure of merit ZT of 0.46 at

705 K was observed for $Pb_5Bi_6Se_{14}$ in the in-plane direction. Future reduction in κ_{at} through increasing complexity of crystal structure is probably achievable by the crystal structural evolution enabled by the homologous series. The thermoelectric power factor can also be further boosted by tuning carrier concentration through doping and increasing carrier mobility through microstructure tuning and single-crystal growth.

Acknowledgements

We thank Mr. Hirotaka Nishiate of AIST for operating the ZEM-3, LFA 457 MicroFlash, and Hall measurement system and Mr. Atsushi Yamamoto of AIST for discussing and reviewing the manuscript. This study was partially supported as part of the Japan-U.S. Cooperation Project for Research and Standardization of Clean Energy Technologies funded by the Ministry of Economy, Trade and Industry (METI). The work in AIST was supported by JSPS KAKENHI Grant Number 25420699. Work at Argonne is supported by the U.S. Department of Energy, Office of Sciences, Materials Sciences and Engineering Division under Contract No. DE-AC02-06CH11357.

Supplementary Information

The sintered mass density, room-temperature Hall coefficient, thermal diffusivity, heat capacity, and scanning electron microscopy micrographs of $Pb_5Bi_6Se_{14}$, $Pb_3Bi_2S_6$, and $PbBi_2S_4$ are available.

Corresponding Author

m-kanatzidis@northwestern.edu (M.G.K)

Notes

The authors declare that they have no competing financial interests.

Author Contributions

M.O. and M.G.K. designed the project. M.O. and D.Y.C synthesized the samples. M.O. and M.K. sintered the samples, performed the XRD and SEM experiments, and investigated the electrical and thermal properties. M.O. D.Y.C, and M.G.K. analyzed the results and wrote the manuscript.

References

[1] G.J. Snyder and E.S. Toberer, *Nat. Mater.*, 2008, **7**, 105–114.

[2] R. Venkatasubramanian, E. Siivola, T. Colpitts and B. O'Quinn, *Nature*, 2001, **413**, 597–602.

[3] K.F. Hsu, S. Loo, F. Guo, W. Chen, J.S. Dyck, C. Uher, T. Hogan, E.K. Polychroniadis and M.G. Kanatzidis, *Science*, 2004, **303**, 818–821.

[4] J.R. Sootsman, D.Y. Chung and M.G. Kanatzidis, *Angew. Chem. Int. Ed.* 2009**, 48**, 8616–8639

[5] M. G. Kanatzidis, *Chem. Mater.*, 2010, **22**, 648–659.

[6] J.Q. He, M.G. Kanatzidis and V.P. Dravid, *Mater. Today,* 2013, **16***,* 166–176.

[7] C.J. Vineis, A. Shakouri, A. Majumdar and M.G. Kanatzidis, *Adv. Mater.*, 2010, **22**, 3970–3980.

[8] K. Biswas, J.Q. He, Q. Zhang, G. Wang, C. Uher, V.P. Dravid and M.G. Kanatzidis, *Nat. Chem.*, 2011, **3**, 160–166.

[9] K. Nielsch, J. Bachmann, J. Kimling and H. Böttner, *Adv. Energy Mater.*, 2011, **1**, 713–731.

[10] M. Ohta, K. Biswas, S.-H. Lo, J.Q. He, D.Y. Chung, V.P. Dravid and M.G. Kanatzidis, *Adv. Energy Mater.*, 2012, **2**, 1117–1123.

[11] K. Biswas, J.Q. He, I.D. Blum, C.-I. Wu, T.P. Hogan, D.N. Seidman, V.P. Dravid and M.G. Kanatzidis, *Nature*, 2012, 489, 414–418.

[12] J.P. Heremans, M.S. Dresselhaus, L.E. Bell and D.T. Morelli, *Nat. Nanotechnol.*, 2013, **8**, 471–473.

[13] M. Martín-González, O. Caballero-Calero and P. Díaz-Chao, *Renew. Sust. Energ. Rev.*, 2013, **24**, 288–305.

[14] L.D. Zhao, V.P. Dravid and M.G. Kanatzidis, *Energy Environ. Sci.*, 2014, **7**, 251–268.

[15] I. Terasaki, Y. Sasago and K. Uchinokura, *Phys. Rev. B*, 1997, **56**, R12685–R12687.

[16] R. Funahashi, I. Matsubara, H. Ikuta, T. Takeuchi, U. Mizutani and S. Sodeoka, *Jpn. J. Appl. Phys.*, 2000, **39**, L1127–L1129.

[17] K. Koumoto, I. Terasaki and R. Funahashi, *MRS Bull.*, 2006, **31**, 206–210.

[18] K. Koumoto, R. Funahashi, E. Guilmeau, Y. Miyazaki, A. Weidenkaff, Y.F. Wang and C.L. Wan, *J. Am.*

Ceram. Soc., 2013, **96**, 1–23.

[19] E. Guilmeau, Y. Bréard and A. Maignan, *Appl. Phys. Lett.*, 2011, **99**, 052107-1–3.

[20] M. Ohta, S. Satoh, T. Kuzuya, S. Hirai, M. Kunii and A. Yamamoto, *Acta Mater.*, 2012, **60**, 7232–7240.

[21] S. Hébert, W. Kobayashi, H. Muguerra, Y. Bréard, N. Raghavendra, F. Gascoin, E. Guilmeau and A. Maignan, *Phys. Status Solidi A*, 2013, **210**, 69–81.

[22] L.-D. Zhao, S.-H. Lo, Y.S. Zhang, H. Sun, G.J. Tan, C. Uher, C. Wolverton, V.P. Dravid and M.G. Kanatzidis, *Nature*, 2014, **508**, 373–377.

[23] E. Makovicky, *Fortschr. Miner.*, 1981, **59**, 137–190.

[24] A. Mrotzek and M.G. Kanatzidis, *Acc. Chem. Res.*, 2003, **36**, 111–119.

[25] M.G. Kanatzidis, *Acc. Chem. Res.*, 2005, **38**, 361–370.

[26] E. Makovicky, *Rev. Mineral. Geochem.*, 2006, **61**, 7–125.

[27] D.-Y. Chung, K.-S. Choi, L. Iordanidis, J.L. Schindler, P.W. Brazis, C.R. Kannewurf, B.X. Chen , S.Q. Hu, C. Uher and M.G. Kanatzidis, *Chem. Mater.*, 1997, **9**, 3060–3071.

[28] D.-Y. Chung, L. Iordanidis, K.-S. Choi and M.G. Kanatzidis, *Bull. Korean Chem. Soc*., 1998, **19**, 1283–1293.

[29] A. Mrotzek, D.-Y. Chung, T. Hogan and M.G. Kanatzidis, *J. Mater. Chem.*, 2000, **10**, 1667–1672.

[30] L. Iordanidis, P. W. Brazis, Th. Kyratsi, J. Ireland, M. Lane, C.R. Kannewurf, W. Chen, J.S. Dyck, C. Uher, N.A. Ghelani, T. Hogan and M.G. Kanatzidis, *Chem. Mater.*, 2001, **13**, 622–633.

[31] K.-S. Choi, D.-Y. Chung, A. Mrotzek, P. Brazis, C. R. Kannewurf, C. Uher, W. Chen, T. Hogan and M.G. Kanatzidis, *Chem. Mater.*, 2001, **13**, 756–764.

[32] A. Mrotzek, D.-Y. Chung, N. Ghelani, T. Hogan and M.G. Kanatzidis, *Chem. Eur. J.*, 2001, **7**, 1915–1926.

[33] Th. Kyratsi, J.S. Dyck, W. Chen, D.-Y. Chung, C. Uher, K.M. Paraskevopoulos and M.G. Kanatzidis, *J. Appl. Phys.*, 2002, **92**, 965–975.

[34] Th. Kyratsi, D.-Y. Chung, J. R. Ireland, C.R. Kannewurf and M.G. Kanatzidis, *Chem. Mater*., 2003, **15**, 3035–3040.

[35] Th. Kyratsi, E. Hatzikraniotis, M. Paraskevopoulous, J.S. Dyck, H.K. Shin, C. Uher and M.G. Kanatzidis, *J. Appl. Phys.*, 2004, **95**, 4140–4146.

[36] J.-H. Kim, D.-Y. Chung and M.G. Kanatzidis, *Chem. Commun.*, 2006, 1628–1630.

[37] Th. Kyratsi, E. Hatzikraniotis, K.M. Paraskevopoulos, C.D. Malliakas, J.S. Dyck, C. Uher and M.G. Kanatzidis, *J. Appl. Phys.*, 2006, **100**, 123704-1–11.

[38] Th. Kyratsi, I. Kika, E. Hatzikraniotis, K.M. Paraskevopoulos, K. Chrissafis and M.G. Kanatzidis, *J. Alloy. Compd.*, 2009, **474**, 351–357.

[39] D.-Y. Chung, T. Hogan, P. Brazis, M. Rocci-Lane, C. Kannewurf, M. Bastea, C. Uher and M.G. Kanatzidis, *Science*, 2000, **287**, 1024–1027.

[40] D.-Y. Chung, T.P. Hogan, M. Rocci-Lane, P. Brazis, J.R. Ireland, C.R. Kannewurf, M. Bastea, C. Uher and M.G. Kanatzidis, *J. Am. Chem. Soc.*, 2004, **126**, 6414–6428.

[41] D.Y. Chung, C. Uher and M.G. Kanatzidis, *Chem. Mater.*, 2012, **24**, 1854–1863.

[42] K.-F. Hsu, D.-Y. Chung, S. Lal, A. Mrotzek, Th. Kyratsi, T. Hogan and M.G. Kanatzidis, *J. Am. Chem. Soc.*, 2002, 124, 2410–2411.

[43] K.-F. Hsu, S. Lal, T. Hogan and M.G. Kanatzidis, *Chem. Commun.*, 2002, 1380–1381.

[44] V.L. Kuznetsov, L.A. Kuznetsova and D.M. Rowe, *J. Appl. Phys.*, 1999, **85**, 3207–3210.

[45] T. Caillat, C.K. Huang, J.-P. Fleurial, G.J. Snyder and A. Borshchevsky, Proceedings of 19th International Conference on Thermoelectrics, Wales, 2000, pp.151–154.

[46] L.A. Kuznetsova, V.L. Kuznetsov and D.M. Rowe, *J. Phys. Chem. Solids*, 2000, **61**, 1269–1274.

[47] V.L. Kuznetsov, L.A. Kuznetsova and D.M. Rowe, *J. Phys. D: Appl. Phys.*, 2001, **34**, 700–703.

[48] L.E. Shelimova, P.P. Konstantinov, O.G. Karpinskii, E.S. Avilov, M.A. Kretova and V.S. Zemskov, *Inorg. Mater.*, 2004, **40**, 1146–1152.

[49] V.S. Zemskov, L.E. Shelimova, P.P. Konstantinov, E.S. Avilov, M.A. Kretova and I.Yu. Nikhezina, *Inorg. Mater. Appl. Res.*, 2012, **3**, 61–68.

[50] B.A. Kuropatwa and H. Kleinke, *Z. Anorg. Allg. Chem.*, 2012, **638**, 2640–2647.

[51] B.A. Kuropatwa, A. Assoud and H. Kleinke, *Z. Anorg. Allg. Chem.*, 2013, **639**, 2411–2420.

[52] D.L. Medlin and G.J. Snyder, *JOM*, 2013, **65**, 390–400.

[53] E. Matzat, *Acta Cryst.*, 1979, **B35**, 133–136.

[54] Y.G Zhang, A.P. Wilkinson, P.L. Lee, S.D. Shastri, D.M. Shu, D.-Y. Chung, and M.G. Kanatzidis, *J. Appl. Crystallogr.*, 2005, **38**, 433–441.

[55] L.E. Shelimova, O.G. Karpinskii, P.P. Konstantinov, E.S. Avilov, M.A. Kretova, G.U. Lubman, I.Yu. Nikhezina and V.S. Zemskov, *Inorg. Mater.*, 2010, **46**, 120–126.

[56] V.S. Zemskov, L.E. Shelimova, P.P. Konstantinov, E.S. Avilov, M.A. Kretova and I.Y. Nikhezina, *Inorg. Mater. Appl. Res.*, 2011, **2**, 405–413.

[57] L. Fang, C.C. Stoumpos, Y. Jia, A. Glatz, D.Y. Chung, H. Claus, U. Welp, W.-K. Kwok and M. G. Kanatzidis, Phys. Rev. B 2014, 90, 020504(R)-1–020504(R)-5.

[58] E. Makovicky and S. Karup-Møller, *Neues. Jb. Miner. Abh.*, 1977, **130**, 264–287.

[59] E. Makovicky and S. Karup-Møller, *Neues. Jb. Miner. Abh.*, 1977, **131**, 56–82.

[60] E. Makovicky, *Neues. Jb. Miner. Abh.*, 1977, **131**, 187–207.

[61] A. Skowron and R.J.D. Tilley, *J. Solid State Chem.*, 1989, **78**, 84–92.

[62] Y. Iitaka and W. Nowacki, *Acta Crystallogr.*, 1962, **15**, 691–698.

[63] Y. Takéuchi. J. Takagi and T. Yamanaka, *Z. Kristall.*, 1974, **140**, 249–272.

[64] R.J.D. Tilley and A.C. Wright, *J. Solid State Chem.*, 1986, **65**, 45–62.

[65] A. Mrotzek and M.G. Kanatzidis, *Inorg. Chem.*, 2003, **42**, 7200–7206.

[66] P. Jood, M. Ohta, H. Nishiate, A. Yamamoto, O.I. Lebedev, D. Berthebaud, K. Suekuni and M. Kuni, *Chem. Mater.*, 2014, **26**, 2684–2692.

[67] F.K. Lotgering, *J. Inorg. Nucl. Chem.*, 1959, **9**, 113–123.

[68] M. Cutler, J.F. Leavy and R.L. Fitzpatrick, *Phys. Rev.*, 1964, **133**, A1143–A1152.

[69] A.F. May, J.-P. Fleurial and G.J. Snyder, *Phys. Rev.*, 2008, **78**, 125205-1–125205-12.

[70] O.L.Anderson, *J. Phys. Chem. Solids*, 1963, **24**, 909–917.

[71] K. Kurosaki, A. Kosuga, H. Muta, M. Uno and S. Yamanaka, *Appl. Phys. Lett*, 2005, **87**, 061919-1–061919-3.

[72] Y.-L. Pei, J.Q. He, J.-F. Li, F. Li, Q. Liu, W. Pan, C. Barreteau, D. Berardan, N. Dragoe and L.-D. Zhao, *NPG Asia Materials*, 2013, **5**, e47-1– e47-9.

[73] T. Zhou, B. Lenoir, M. Colin, A. Dauscher, R. Al Rahal Al Orabi, P. Gougeon, M. Potel and Emmanuel Guilmeau, *Appl. Phys. Lett*, 2011, **98**, 162106-1–162106-3.

[74] J.Y. Cho, X. Shi, J.R. Salvador, G.P. Meisner, J. Yang, H. Wang, A.A. Wereszczak, X. Zhou and C. Uher, *Phys. Rev.*, 2011, **84**, 085207-1–085207-9.

[75] D.G. Cahill, S.K. Watson and R.O. Pohl, *Phys. Rev. B*, 1992, **46**, 6131–6140.

[76] A. Olvera, G. Shi, H. Djieutedjeu, A. Page, C. Uher, E. Kioupakis and P.F. P. Poudeu, *Inorg Chem, in press,* DOI: 10.1021/ic501327u.

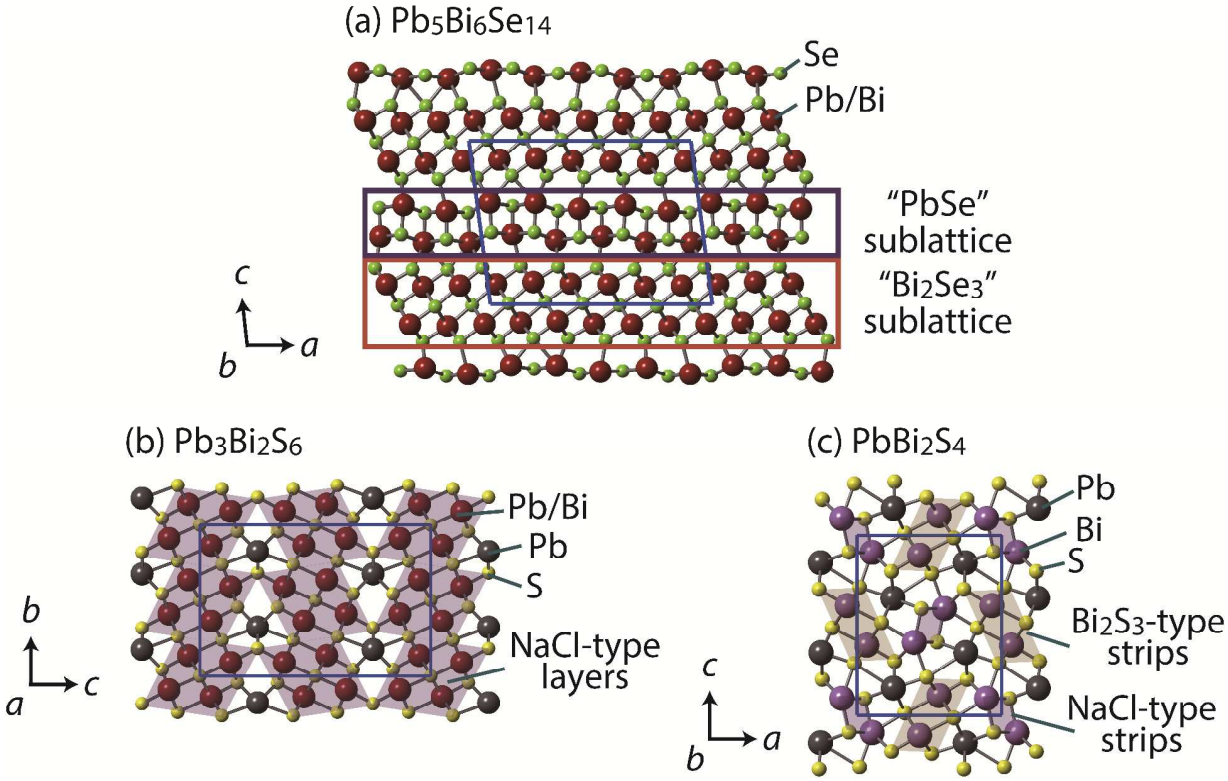

Figure 1.

Crystal structures of (a) a member of the cannizzarite homologous series $Pb_5Bi_6Se_{14}$, (b) a member of the lillianite homologous series $Pb_3Bi_2S_6$, and (c) a member of the galenobismuthite series $PbBi_2S_4$. Size of atoms in this figure is arbitrary for better view.

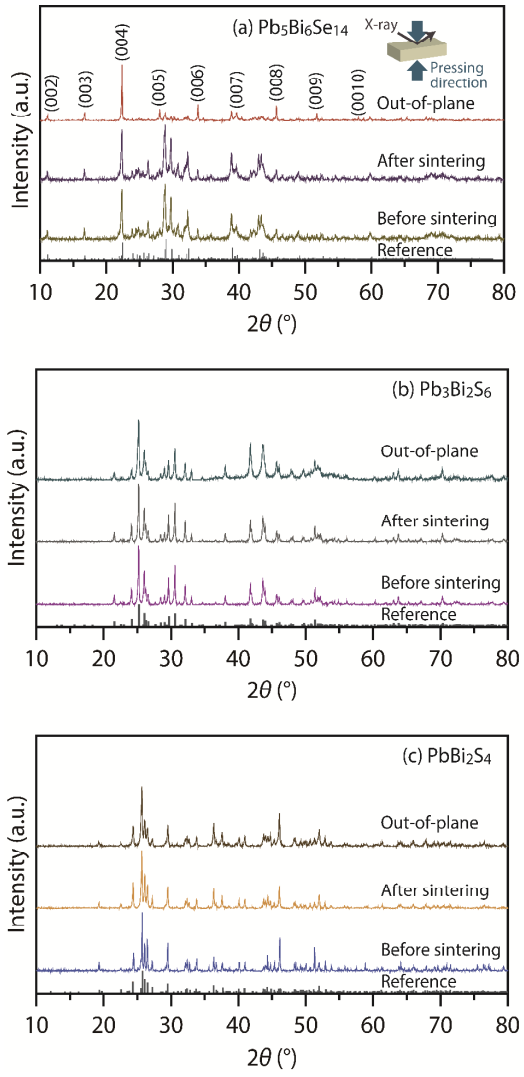

Figure 2.

Powder X-ray diffraction (XRD) patterns for (a) $Pb_5Bi_6Se_{14}$, (b) $Pb_3Bi_2S_6$, and (c) $PbBi_2S_4$ before sintering and after sintering and out-of-plane XRD patterns of the sintered compacts. The sintered compacts were hand-ground to measure the powder XRD patterns. References are taken from Ref.45 for $Pb_5Bi_6Se_{14}$, Ref.51 for $Pb_3Bi_2S_6$, and Ref.54 for $PbBi_2S_4$.

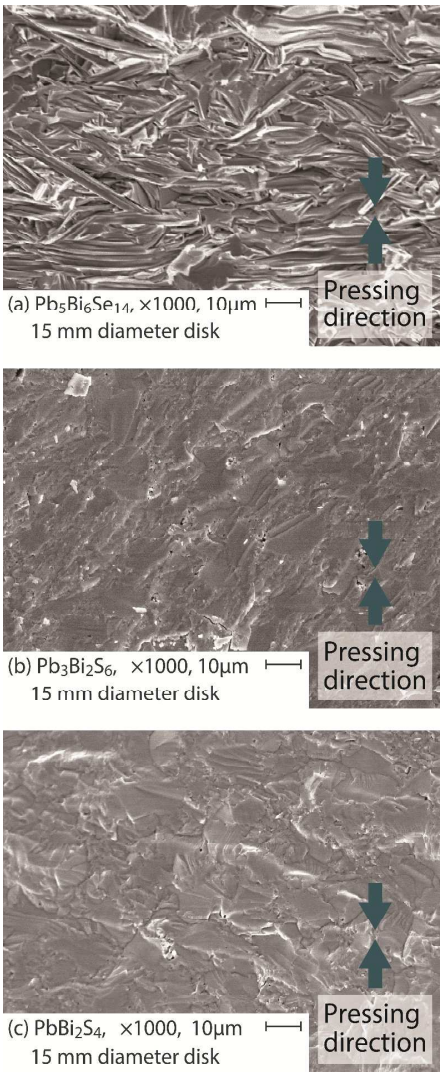

Figure 3.

Scanning electron microscopy micrographs of the fractured section for the sintered compacts of (a) $Pb_5Bi_6Se_{14}$, (b) $Pb_3Bi_2S_6$, and (c) $PbBi_2S_4$. The disk-type samples (~15 mm diameter × ~2 mm thickness) were fractured parallel to the pressing direction.

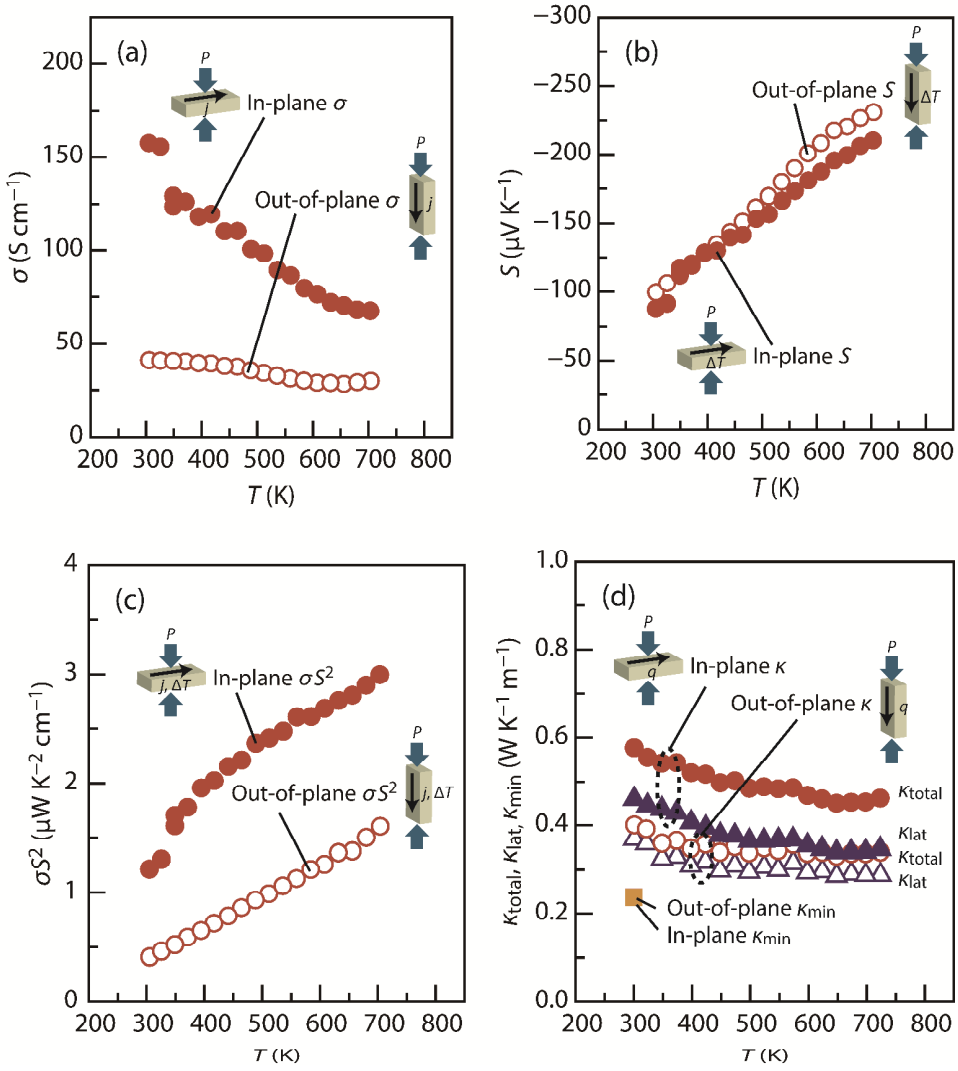

Figure 4.

Temperature dependence of the (a) electrical conductivity (σ), (b) Seebeck coefficient (S), (c) power factor (σS^2), and (d) total thermal conductivity (κ_{total}) for the sintered compacts of $Pb_5Bi_6Se_{14}$ measured perpendicular (in-plane) and parallel (out-of-plane) to the pressing direction. The lattice thermal conductivity (κ_{lat}) and theoretical minimum limit of lattice thermal conductivity (κ_{min}) are also plotted in (d).

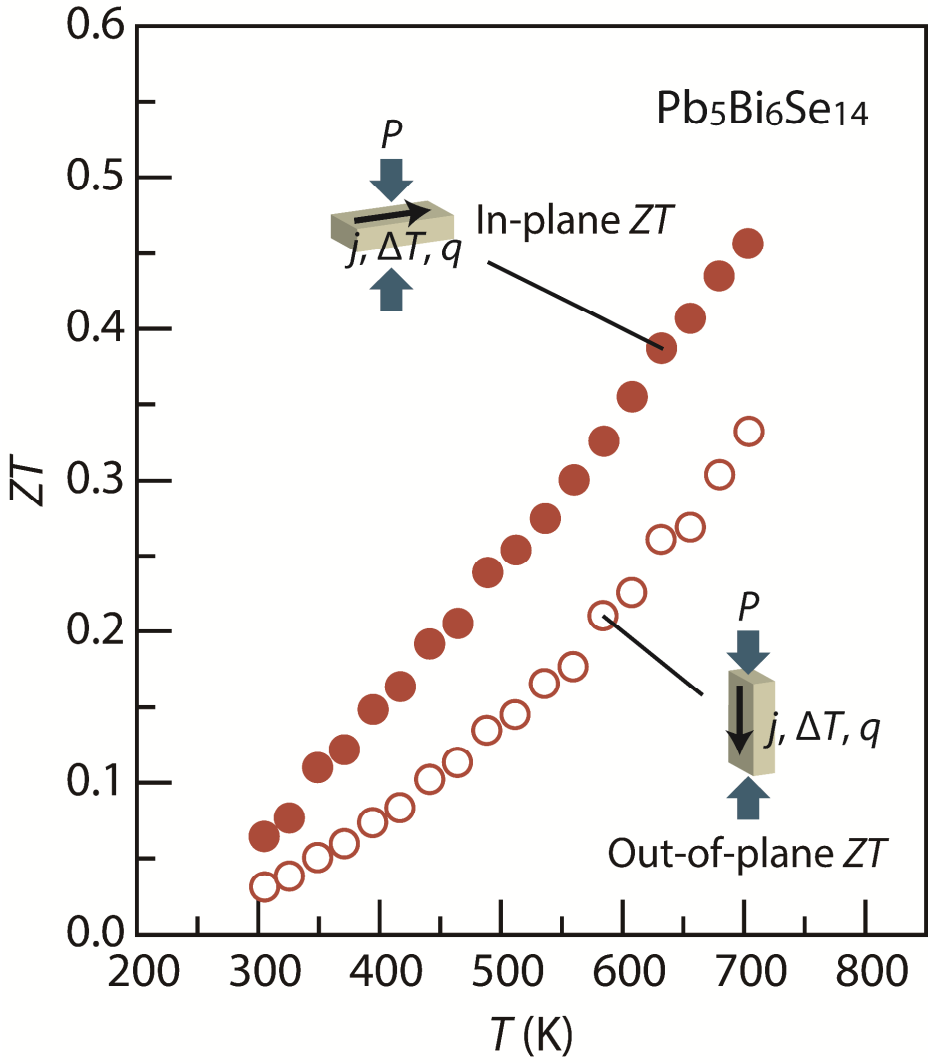

Figure 5.

Temperature dependence of the thermoelectric figure of merit (*ZT*) for the sintered compacts of $Pb_5Bi_6Se_{14}$ perpendicular (in-plane) and parallel (out-of-plane) to the pressing direction.

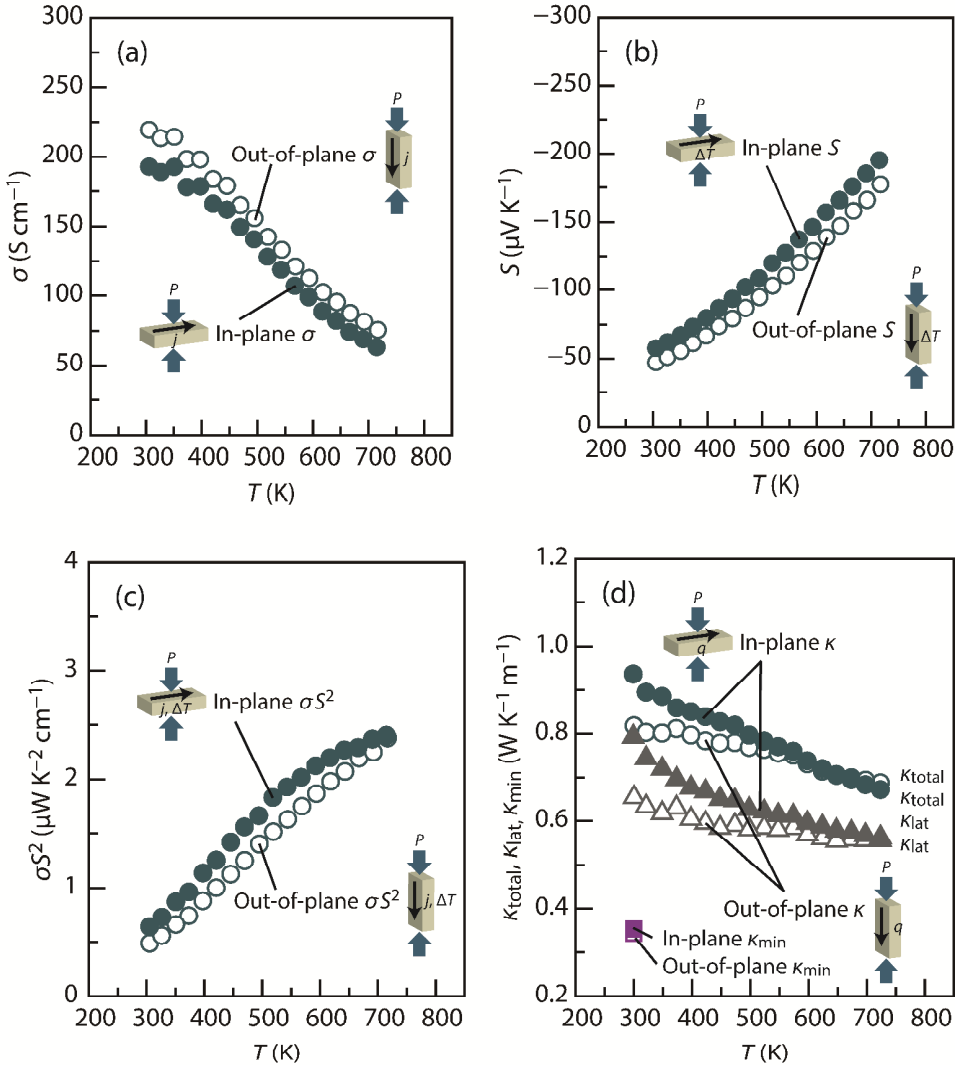

Figure 6.

Temperature dependence of the (a) electrical conductivity (σ), (b) Seebeck coefficient (S), (c) power factor (σS^2), and (d) total thermal conductivity (κ_{total}) for the sintered compacts of $Pb_3Bi_2S_6$ measured perpendicular (in-plane) and parallel (out-of-plane) to the pressing direction. The lattice thermal conductivity (κ_{lat}) and theoretical minimum limit of lattice thermal conductivity (κ_{min}) are also plotted in (d).

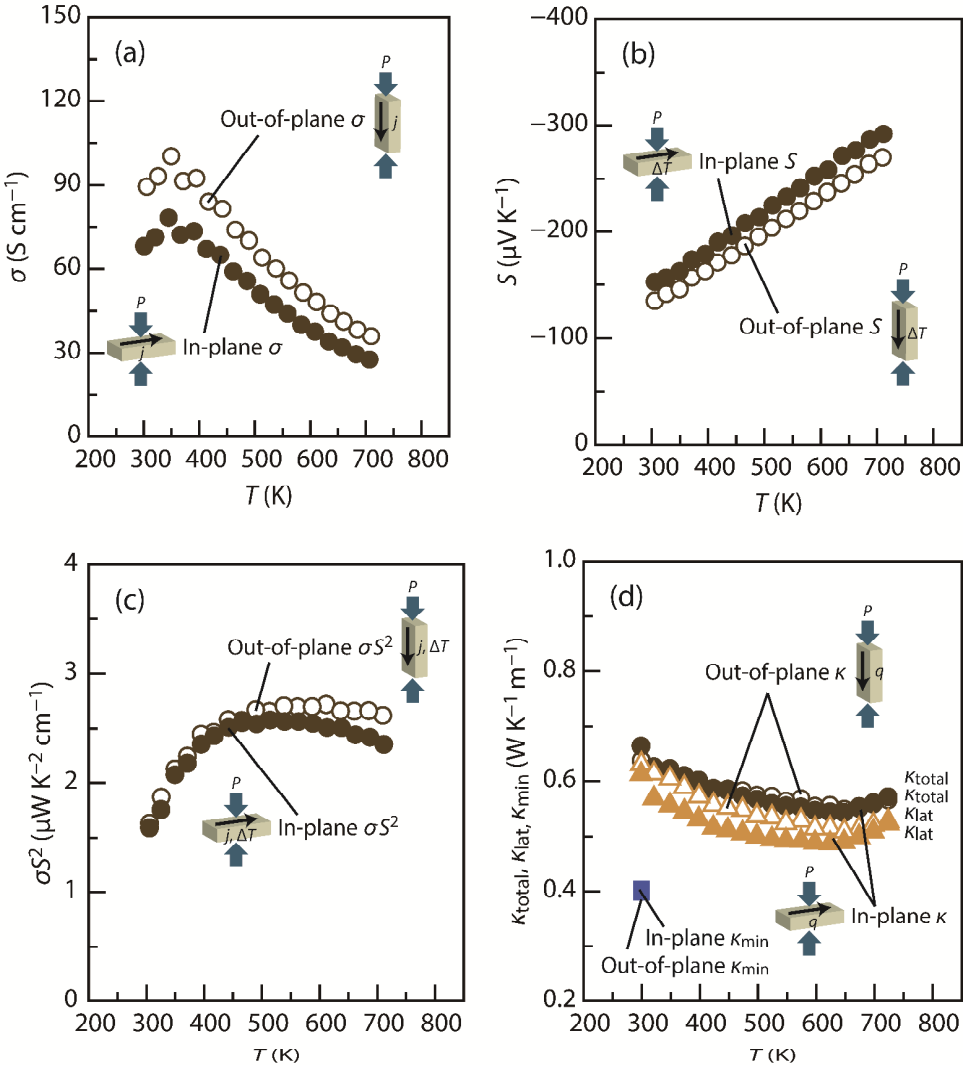

Figure 7.

Temperature dependence of the (a) electrical conductivity (σ), (b) Seebeck coefficient (S), (c) power factor (σS^2), and (d) total thermal conductivity (κ_{total}) for the sintered compacts of $PbBi_2S_4$ measured perpendicular (in-plane) and parallel (out-of-plane) to the pressing direction. The lattice thermal conductivity (κ_{lat}) and theoretical minimum limit of lattice thermal conductivity (κ_{min}) are also plotted in (d).

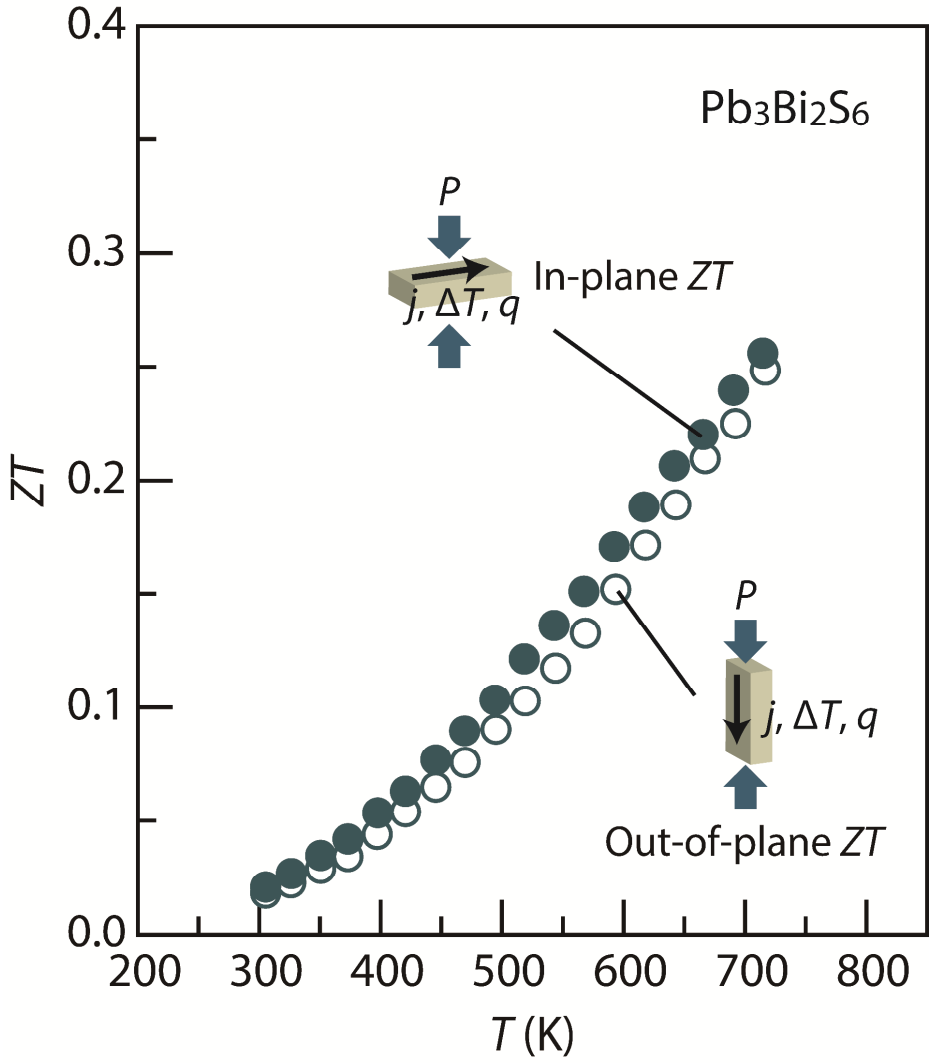

Figure 8.

Temperature dependence of the thermoelectric figure of merit (*ZT*) for the sintered compacts of $Pb_3Bi_2S_6$ perpendicular (in-plane) and parallel (out-of-plane) to the pressing direction.

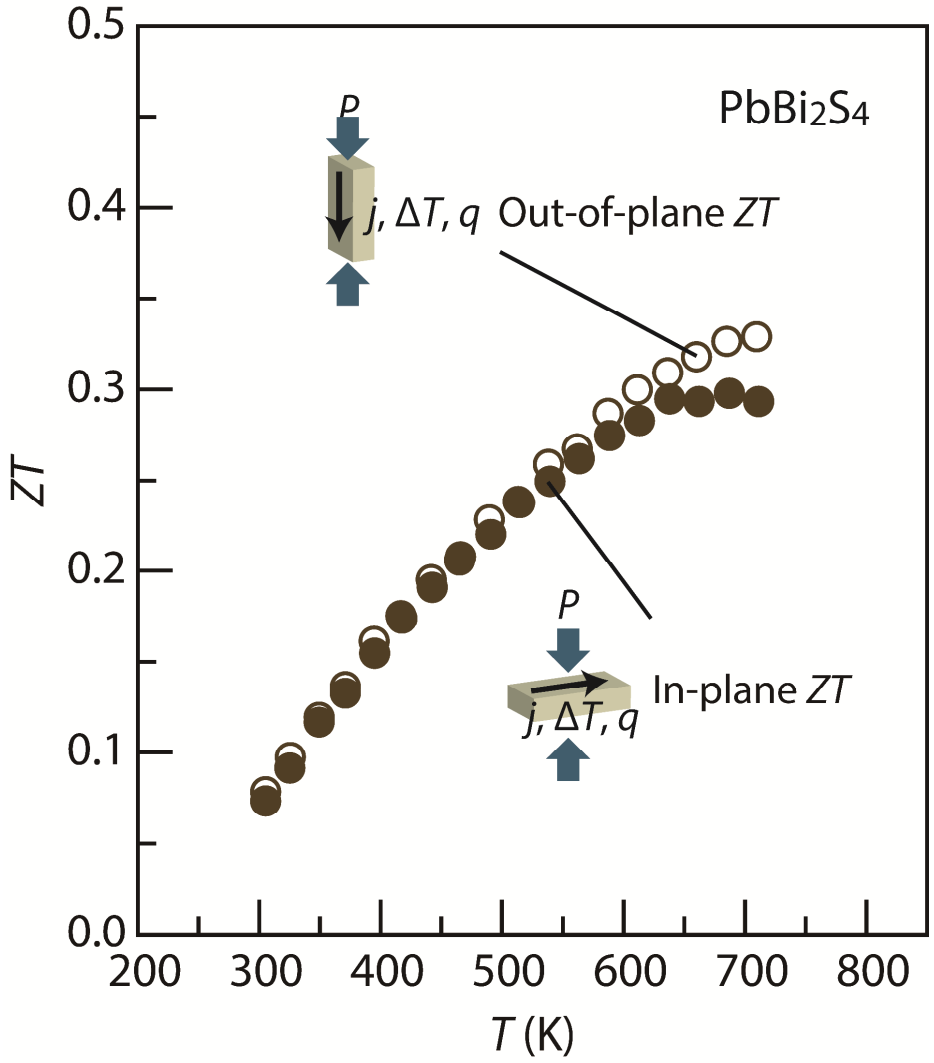

Figure 9.

Temperature dependence of the thermoelectric figure of merit (*ZT*) for the sintered compacts of $PbBi_2S_4$ perpendicular (in-plane) and parallel (out-of-plane) to the pressing direction.

Table 1.

Lattice parameters calculated from powder XRD patterns of $Pb_5Bi_6Se_{14}$, $Pb_3Bi_2S_6$, and $PbBi_2S_4$ before and after sintering.

Sample		Lattice parameter
$Pb_5Bi_6Se_{14}$	before sintering	a = 2.1537 nm, b = 0.4202 nm, c = 1.6028 nm, β = 97.34°
	after sintering	a = 2.1540 nm, b = 0.4206 nm, c = 1.6047 nm, β = 97.39°
	Ref. [54]	a = 2.15689(3) nm, b = 0.420148(4) nm, c = 1.60096(3) nm, β = 97.537(1)°
$Pb_3Bi_2Se_6$	before sintering	a = 0.4116 nm, b = 1.3571 nm, c = 2.0679 nm
	after sintering	a = 0.4119 nm, b = 1.3576 nm, c = 2.0663 nm
	Ref. [61]	a = 0.4111(1) nm, b = 1.3540(4) nm, c = 2.0654(4) nm
$PbBi_2S_4$	before sintering	a = 1.1789 nm, b = 0.4088 nm, c = 1.4572 nm
	after sintering	a = 1.1812 nm, b = 0.4085 nm, c = 1.4568 nm
	Ref. [64]	a = 1.1753 nm, b = 0.4087 nm, c = 1.4612 nm

Table 2.

Room-temperature carrier concentration (n) and carrier mobility (μ) of the sintered compacts of $Pb_5Bi_6Se_{14}$, $Pb_3Bi_2S_6$, and $PbBi_2S_4$.

Sample		n (cm^{-3})	μ ($cm^2\ V^{-1}\ s^{-1}$)
$Pb_5Bi_6Se_{14}$	in-plane	4.8×10^{19}	20
	out-of-plane		5.4
$Pb_3Bi_2S_6$	in-plane	1.2×10^{20}	9.9
	out-of-plane		11
$PbBi_2S_4$	in-plane	4.6×10^{19}	9.3
	out-of-plane		12

Table 3.

Room-temperature longitudinal sound velocity (v_l), transverse sound velocity (v_t), average sound velocity (v_a), mean free path of phonon (l_p), and Debye temperature associated with the longitudinal (Θ_l) and transverse modes (Θ_t) of the sintered compacts of $Pb_5Bi_6Se_{14}$, $Pb_3Bi_2S_6$, and $PbBi_2S_4$.

Sample		v_l (m s^{-1})	v_t (m s^{-1})	v_a (m s^{-1})$_i$	l_p (nm)	Θ_l (K)	Θ_t (K)
$Pb_5Bi_6Se_{14}$	in-plane	2720	1220	1380	0.8	260	120
	out-of-plane	2740	1210	1370	0.6	270	120
$Pb_3Bi_2S_6$	in-plane	3160	1590	1780	0.9	320	160
	out-of-plane	3090	1580	1770	0.7	310	160
$PbBi_2S_4$	in-plane	3240	1780	1980	0.6	330	180
	out-of-plane	3210	1770	1970	0.6	330	180

Table 4.

Room-temperature thermoelectric properties of the sintered sample of $Pb_5Bi_6Se_{14}$ observed in this study and the melt-grown ingot of $Pb_5Bi_6Se_{14}$ observed in the previous study.

Direction	n (cm^{-3})	σ (S cm^{-1})	S ($\mu V\ K^{-1}$)	σS^2 ($\mu W\ K^{-2}\ cm^{-1}$)	κ_{total} ($W\ K^{-1}\ cm^{-1}$)	κ_{lat} ($W\ K^{-1}\ cm^{-1}$)	ZT	Reference
In-plane	4.8×10^{19}	157	88	120	0.58	0.48	0.06	This study
Out-of-plane		41.2	100	41	0.40	0.37	0.03	This study
Unknown	8.6×10^{19}	454	28	36	1.0	0.72	0.01	[55]

Graphical abstract

We demonstrate a notable power factor and an extremely low lattice thermal conductivity in $Pb_5Bi_6Se_{14}$, a member of the cannizzarite homologous series; $Pb_3Bi_2S_6$, a member of the lillianite homologous series; and $PbBi_2S_4$, a member of the galenobismuthite series.